Journal of Power Sources 185 (2008) 1233–1246

Contents lists available at ScienceDirect

Journal of Power Sources

journal homepage: www.elsevier.com/locate/jpowsour

A two-dimensional two-phase mass transport model for direct methanol fuel cells adopting a modified agglomerate approach

Zheng Miao, Ya-Ling He*, Xiang-Lin Li, Jin-Qiang Zou

State Key Laboratory of Multiphase Flow in Power Engineering, School of Energy and Power Engineering, Xi'an Jiaotong University, Xi'an, Shaanxi 710049, China

ARTICLE INFO

Article history:
Received 21 April 2008
Received in revised form 31 May 2008
Accepted 4 June 2008
Available online 12 June 2008

Keywords:
Direct methanol fuel cells
Two-phase model
Agglomerate model
Methanol crossover
Electrochemical reaction rate

ABSTRACT

A two-dimensional two-phase mass transport model for liquid-feed direct methanol fuel cells (DMFCs) is presented in this paper. The fluid flow and mass transport across the membrane electrode assembly (MEA) is formulated based on the classical multiphase flow theory in the porous media. The modeling of mass transport in the catalyst layers (CLs) and membrane is given more attentions. The effect of the two-dimensional migration of protons in the electrolyte phase on the liquid flow behavior is considered. Water and methanol crossovers through the membrane are implicitly calculated in the governing equations of momentum and methanol concentration. A modified agglomerate model is developed to characterize the microstructure of the CLs. A self-written computer code is used to solve the inherently coupled differential governing equations. Then this model is applied to investigate the mechanisms of species transport and the distributions of the species concentrations, overpotential and the electrochemical reaction rates in CLs. The effects of radius and overlapping angle of agglomerates on cell performance are also explored in this work.

1. Introduction

The liquid-feed direct methanol fuel cell (DMFC) is presently regarded as one of the most promising candidates to replace the conventional batteries, especially those used for portable electronic devices [1]. However, the commercialization of DMFCs is still hindered by several technological problems [2], such as low electro-activity of methanol oxidation on the surface of anode catalyst particles, substantial methanol crossover through the proton exchange membrane (MEM) from the anode to the cathode and the water management to prevent severe cathode flooding. Extensive efforts have been made to solve these problems and also much work has been focused on the fundamentals of the DMFC system, among which the computational modeling of DMFCs played an important role. Modeling was regarded as a powerful and economical tool to investigate the intrinsically coupled processes in a DMFC which are difficult to be studied by experiments.

Over the past decade, many mathematical models have been developed [3–19], which include single-phase models [3–11] and two-phase models [12–19]. Most of the previous published models for DMFCs are based on the single-phase flow assumption and several significant conclusions have been obtained according to the analysis of the distribution of species concentration, the effect of operation conditions on cell performance and so on. However, the in situ visualization research of DMFC [20–23] revealed that the fluid flow in the DMFC is not a simple single-phase process, there is coexisting liquid and gas two-phase flow behavior in the flow channel because of the generation of gaseous carbon dioxide in the anode catalyst layer (ACL) and formation of liquid water in the cathode catalyst layer (CCL). The significant effects of the two-phase flow behavior on the mass transport processes and on the cell performance [12,17,19] demand the development of two-phase mathematical models.

Most of the published two-phase models are based on the classical multiphase flow theory with assumptions and simplifications. Wang and Wang [12] developed a two-phase model for DMFCs based on the mixture multiphase flow approach for the porous regions and the drift flux model for the two-phase flow in channels of the flow-field plates. The liquid and gas mixture is assumed to be a homogeneous fluid at the thermodynamic equilibrium condition, and its properties can be derived from the parameters of each individual phase based on certain mixing rules. The CLs in this model are treated as infinitely thin interfaces. Ge and Liu [13] presented a three-dimensional, two-phase mathematical model adopting the general momentum conservation equations with a source term accounting for the forces exerted on the fluid by the solid matrix of the porous media. The CLs are treated as porous regions with finite width. Differential equations are solved by the CFD technique on the single computational domain consisting of seven layers: flow

* Corresponding author. Tel.: +86 29 8266 5930; fax: +86 29 8266 9106.
E-mail address: yalinghe@mail.xjtu.edu.cn (Y.-L. He).

0378-7753/$ – see front matter © 2008 Elsevier B.V. All rights reserved.
doi:10.1016/j.jpowsour.2008.06.007

channels, diffusion layers (DLs), CLs and the MEM. Divisek et al. [14] developed a two-dimensional, two-phase mathematical model for a DMFC by regarding the DLs as water-gas systems in the pore space with saturation permeability varying according to the capillary effects. A new parameterization of the relationship between capillary pressure and saturation is introduced in their work. In particular, the electrochemical reactions are split up into reaction chains to obtain a more precise expression of the electrochemical reaction rates.

From the models mentioned above, it can be concluded that the mass transport processes in the CLs and in the MEM are not fully explored. Many researchers treated the CLs as either infinitely thin interfaces or pseudo-homogeneous porous media to simplify their models. The microstructure of the CLs is ignored and the simulations of potential and velocities in electrolyte-phase-region (CLs and MEM) are simplified. Studies of the microstructure of CLs by high-resolution scanning electron microscopy (HR-SEM) [24] showed that the CLs consist of randomly distributed pores and agglomerates of much smaller carbon-based catalyst particles. Computational model invoking agglomerate approach to model the mass transport and electrochemical reaction processes in the CLs is first developed for the alkaline oxygen electrode by Giner and Hunter [25] with the concept of "flooded agglomerates". In the case of PEM fuel cells, researchers have also studied various phenomena in the CLs based on the agglomerate model [26–30].

However, only a few literatures adopted the agglomerate model to characterize the CLs of the DMFCs. Nordlund and Lindbergh [31] modeled the anode of a DMFC based on an agglomerate model for the mass transport and electrochemical reaction processes of methanol and carbon dioxide in the ACL. Modeling results showed that the concentration profiles within the agglomerates on the anode can be neglected so that the model can be simplified. In their model, they assumed isobaric condition in the electrode and that carbon dioxide is dissolved in the water. Yang and Zhao [15] presented a two-dimensional, two-phase model for liquid-feed DMFCs with a micro-agglomerate model developed for the CCL. The oxygen transfer processes from the gas pores to the active sites were modeled by considering the agglomerate covered by a liquid film.

Some simplifications used in the two-phase mass transport models above, including models that adopted the agglomerate approach, can be collected as follows: (1) The overpotential in the CLs is always assumed to distribute uniform as the proton migration process in the electrolyte phase of CLs is not considered. The electrochemical reaction rates are very sensitive to the overpotential, so it is worth investigating the effect of overpotential on the distribution of electrochemical reaction rates in the CLs; (2) Both water and methanol crossover rates are explicitly calculated by expressions that account for the combination of diffusion, back convection and electro-osmotic drag. Consequently, the two-dimensional dispersion of water and methanol in the MEM is simplified as one-dimensional permeation process through the MEM because only the variables at the two boundaries, interfaces between the CLs and the MEM, can be used in these expressions; (3) The 'parasitic' methanol current density is dictated by the methanol crossover rate. Since the mass transport of methanol in the CCL is not considered, the distribution of the 'parasitic' current cannot be obtained; (4) The geometry of the spherical agglomerate with a Nafion or water coating is always adopted in the agglomerate models. However, the Nafion coating or water film covering outside of the spherical agglomerate will block the access of electrons, so a more realistic geometry of the agglomerate should be developed to satisfy the common recognition that the CLs should supply access for all the three phases: reactants, protons and electrons.

The objective of this work is to develop a two-dimensional, two-phase mass transport model for a liquid feed DMFC which can provide a useful insight into the mechanisms of species transport and more realistic distributions of variable fields in the CLs. In this model, the local overpotential in the CLs are derived from the current conservation equations by considering the transport of electrons in the carbon phase and protons in the electrolyte phase. Water and methanol crossovers through the MEM are taken into account by incorporating the MEM into the computational domains of the momentum conservation equations and the species equation for methanol. The 'parasitic' current density in the CCL is calculated by a Tafel-like expression similar to that in the anode side and a modified agglomerate model is applied for the CCL.

2. Mathematical model

The two-dimensional computational domain, as enclosed by the dashed lines in Fig. 1, represents the geometry of a complete MEA, which consists of anode diffusion layer (ADL), ACL, MEM, CCL and cathode diffusion layer (CDL). Since the parallel flow-field plates are used in the DMFC, only a periodic unit: part of the MEA sandwiched by a flow channel and two hemi-ribs is considered in this model. Governing equations are elaborated below.

2.1. Potential governing equations

In a DMFC, protons and electrons are generated in the ACL and combined in the CCL. The motion of protons and electrons obeys the Ohm's law and the current conservation equation:

$$\mathbf{I} = \nabla(\sigma\varphi) \tag{1}$$

$$\nabla \cdot \mathbf{I} = i \tag{2}$$

where $\mathbf{I}$ is the current vector and i is the generation rate of current; σ is the electric conductivity of materials and φ is the electric potential.

Following the concept of electric potential of the membrane phase φ_m (or electrolyte phase) and solid phases φ_s (or carbon phase) introduced by Kulikovsky [6], we can obtain potential governing equations by substituting Eq. (1) into Eq. (2):

$$\nabla \cdot (\sigma_m \nabla \varphi_m) = i_m \tag{3}$$

$$\nabla \cdot (\sigma_s \nabla \varphi_s) = i_s \tag{4}$$

where σ_m and σ_s denote the conductivity of electrolyte and carbon phases; i_m and i_s represent the generation rates of protons and electrons respectively. In this model, the ACL, MEM and CCL are

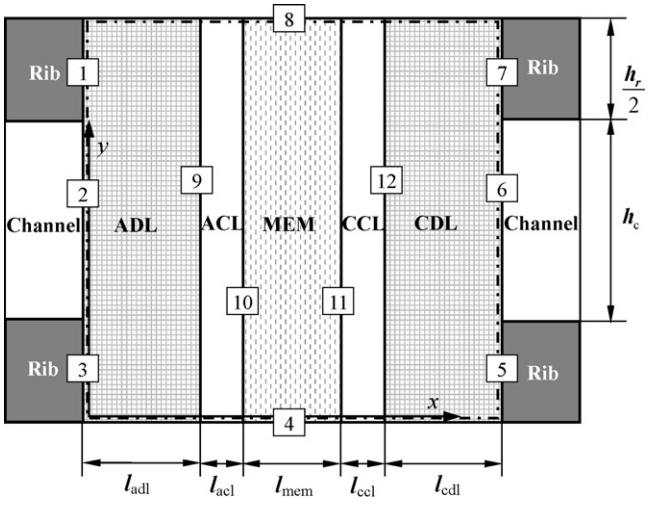

Fig. 1. Schematic of the computational domain of a liquid-feed DMFC.

specified as the electrolyte-phase-region, which means the computational domain of electrolyte phase potential.

2.2. Velocity and pressure equations for gas and liquid phases

In the classical two-phase flow theory in a porous media, the mass conservation equations can be given as follows:

$$\nabla \cdot (\rho_g \mathbf{u}_g) = \dot{m}_g \tag{5}$$

$$\nabla \cdot (\rho_l \mathbf{u}_l) = \dot{m}_l \tag{6}$$

where ρ, $\mathbf{u}$ and $\dot{m}$ represent the density, the superficial velocity vector and the mass generation rate.

2.2.1. Velocity and pressure of the gas phase

Gas phase in the DMFC is a multi-component mixture, including carbon dioxide, water vapor, methanol vapor and oxygen when pure oxygen is supplied in the cathode flow channel (CFC). In order to simplify the model, the commonly used assumptions are also adopted in the present model that the transport of methanol in gas phase is neglected [13,15,18] and carbon dioxide produced by the methanol oxidation reaction (MOR) on the anode and methanol direct oxidation reaction (MDOR) on the cathode only exists in the gas phase [15–19]. The convective transport of gases is caused by the pressure gradient of the gas phase, so the expression of gas velocity is given as [15]:

$$\mathbf{u}_g = -K \frac{k_{rg}}{\mu_g} \nabla p_g \tag{7}$$

where K represents the absolute permeability of the porous media, k_{rg} represents the relative permeability of gas phase, μ_g and p_g are the viscosity and pressure of the gas phase. By substituting Eq. (7) into Eq. (5), the governing equation of gas phase pressure can be obtained in the following form:

$$\nabla \cdot \left[\left(-K \frac{\rho_g k_{rg}}{\mu_g} \right) \nabla p_g \right] = \dot{m}_g \tag{8}$$

2.2.2. Velocity and pressure of the liquid phase

In a liquid-feed DMFC, the dilute methanol aqueous solution is supplied in the anode flow channel (AFC). As protons produced on the anode exist in the form of hydrated ions, the migration of protons in an electrical field will lead to the bulk motion of liquid phase. So it can be seen that not only the gradient of liquid pressure but also electro-osmotic drag force contributes to the liquid velocity. The expression of liquid velocity similar to that used in literature [12] is applied:

$$\mathbf{u}_l = -K \frac{k_{rl}}{\mu_l} \nabla p_l + \frac{n_d M}{\rho_l} \frac{\mathbf{I}}{F} \tag{9}$$

where n_d represents the electro-osmotic drag coefficient of water. F is the Faraday's constant. M is equal to the water molecular weight M_W due to the dilute solution assumption. Substituting Eq. (9) into Eq. (6), with the aid of Eqs. (1)–(3), we obtain:

$$\nabla \cdot \left[\left(-K \frac{\rho_l k_{rl}}{\mu_l} \right) \nabla p_l \right] = \dot{m}_l - \frac{n_d M_W}{F} i_m \tag{10}$$

The relative permeability of gas phase k_{rg} and liquid phase k_{rl} in Eqs. (7)–(10) can be formulated by the liquid saturation alone [12]:

$$k_{rl} = s^3 \tag{11}$$

$$k_{rg} = (1-s)^3 \tag{12}$$

The mass conservation and momentum conservation in the DMFC can be satisfied by solving Eqs. (7)–(10) iteratively.

2.3. Liquid saturation in the porous media

The liquid pressure in the porous media is not equal to the gas pressure because of the capillary effect. The pressure difference between these two phases is defined as capillary pressure. The Leverette function [32,33] is adopted to describe the relationship between the liquid saturation and the capillary pressure.

$$p_c = p_g - p_l = \sigma \cos\theta_c \left(\frac{\varepsilon}{K} \right)^{0.5} J(s) \tag{13}$$

$$J(s) = \begin{cases} 1.417(1-s) - 2.12(^1 + 1.263(^1 & 0^\circ \le \theta_c < 90^\circ \\ 1.417s - 2.12s^2 + 1.263s^3 & 90^\circ \le \theta_c < 180^\circ \end{cases} \tag{14}$$

where σ, θ_c and ε denote the surface tension of the liquid phase, the contact angle between the liquid phase and the solid wall, and the porosity of the porous media respectively. Substituting Eq. (13) into Eqs. (8) and (10) yields:

$$\nabla \cdot \left[\left(K \frac{\rho_l k_{rl}}{\mu_l} \right) \left(\frac{dp_c}{ds} \right) \nabla s \right] = \dot{m}_l + \frac{n_d M_W}{F} i_m - \frac{\rho_l k_{rl} \mu_g}{\rho_g k_{rg} \mu_l} \dot{m}_g \quad \text{(ADL, ACL)} \tag{15}$$

$$\nabla \cdot \left[\left(-K \frac{\rho_g k_{rg}}{\mu_g} \right) \left(\frac{dp_c}{ds} \right) \nabla s \right] = \dot{m}_g - \frac{\rho_g k_{rg} \mu_l}{\rho_l k_{rl} \mu_g} \left(\dot{m}_l + \frac{n_d M_W}{F} i_m \right) \quad \text{(CDL, CCL)} \tag{16}$$

In order to guarantee the robustness of the self-written code and smaller interpolation error, governing equations for liquid saturation are restricted to the specified computational domains indicated in Eqs. (15) and (16).

2.4. Concentration of species

We now turn our attention to the mass transport of different species, including methanol, oxygen and water vapor, in the porous media. The general species conservation equations [34] can be written as follows:

$$\nabla \cdot (\mathbf{u}_i C_i) = \nabla \cdot (D_i^{eff} \nabla C_i) + \dot{R}_i \tag{17}$$

where C_i and $\dot{R}_i$ represent the concentration and the molar generation rate of species i. D_i^{eff} is the effective diffusion coefficient of species i corrected with the porosity and liquid saturation. $\mathbf{u}_i$ stands for the velocity of liquid or gas phase and can be set as the value below for different species:

$$\mathbf{u}_i = \begin{cases} \mathbf{u}_l & CH_3OH \\ \mathbf{u}_g & O_2, H_2O\uparrow \end{cases} \tag{18}$$

where $H_2O\uparrow$ represents the water vapor.

2.5. Electrochemical kinetics

As the mechanisms of the complicated multi-step electrochemical reactions occurring in a DMFC have not been completely understood, the Tafel-like expressions [18] are used for the kinetics of MOR on the anode and oxygen reduction reaction (ORR) on the cathode for simplification.

$$i_a = s A_a i_M^{ref} \left(\frac{C_M \xi_M}{C_M^{ref}} \right)^{\gamma} \exp\left[\frac{\alpha_a F}{RT} (\varphi_{s,a} - \varphi_{m,a}) \right] \tag{19}$$

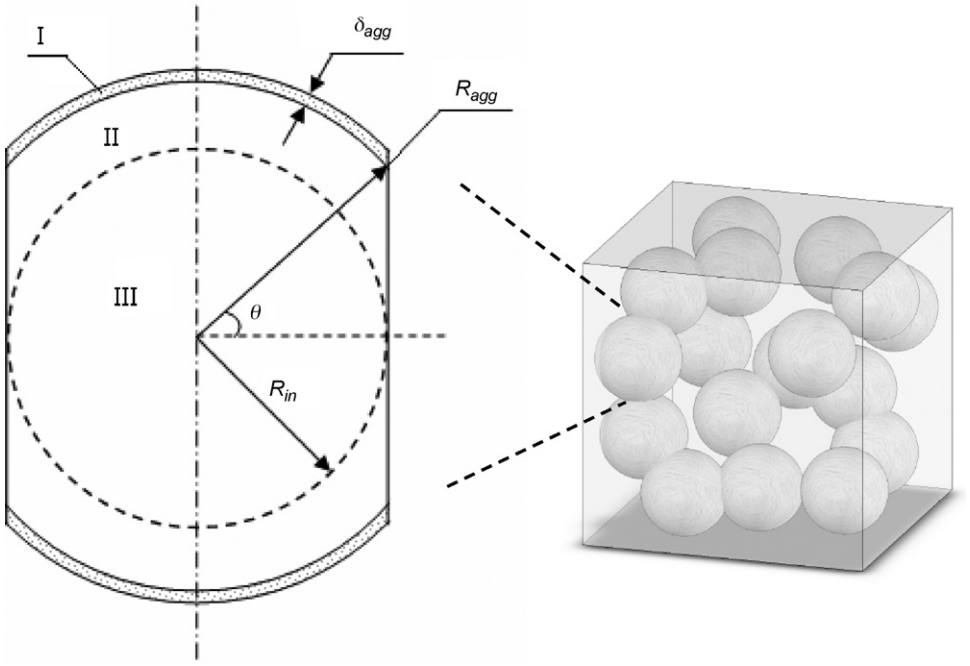

Fig. 2. Sketch of the agglomerate geometry in the CCL.

$$i_c = (1-s)A_c i_{O_2}^{ref}\left(\frac{C_{O_2}\xi_{O_2}}{C_{O_2}^{ref}}\right)\exp\left[\frac{\alpha_c F}{RT}(\varphi_{m,c}-\varphi_{s,c})\right] \quad (20)$$

where C_M and C_{O_2} are the concentrations of methanol and oxygen in the bulk pores of the CLs; C_M^{ref} and $C_{O_2}^{ref}$ are reference concentrations; ξ_M and ξ_{O_2} are correction factors derived from the agglomerate model and will be discussed in detail later. The reaction order γ is determined by the methanol concentration at the active sites of the catalyst particles, $C_M\xi_M$, and can be set as:

$$\gamma = \begin{cases} 0 & C_M\xi_M > C_M^{ref} \\ 1 & C_M\xi_M \le C_M^{ref} \end{cases} \quad (21)$$

The correction factors, ξ_M and ξ_{O_2} in Eqs. (19) and (20), consider effects of the mass transfer resistance induced by agglomerates with a Nafion coating and a overlapping region between two adjacent agglomerates as illustrated in Fig. 2. In the ACL, the Thiele module is very small so that there is no need to account for the concentration difference in the agglomerate [31]. In this model, the correction factor ξ_M = 1.0 is adopted for the ACL.

In the CCL, oxygen in the bulk pores should first dissolves into the Nafion coating. This process can be described by the Henry's law:

$$C_{O_2N} = \frac{C_{O_2}}{k_H} \quad (22)$$

where k_H is the Henry's constant and C_{O_2N} is the concentration of dissolved oxygen at the outer surface of the Nafion coating. It is assumed that the transport of oxygen in the Nafion coating and in the agglomerate is a diffusion dominating process, so that the mass transport of oxygen through the Nafion coating and consumption of oxygen in the agglomerate can be modeled with:

$$\frac{d^2C_{O_2,N}}{dr^2} + \frac{1}{r}\frac{dC_{O_2,N}}{dr} = 0 \quad \text{(Sub-domain I)} \quad (23)$$

$$\frac{d^2C_{O_2,agg}}{dr^2} + \frac{1}{r}\frac{dC_{O_2,agg}}{dr} = \frac{k_v}{D_{O_2,agg}^{eff}}C_{O_2,agg} \quad \text{(Sub-domain II)} \quad (24)$$

$$\frac{d^2C_{O_2,agg}}{dr^2} + \frac{2}{r}\frac{dC_{O_2,agg}}{dr} = \frac{k_v}{D_{O_2,agg}^{eff}}C_{O_2,agg} \quad \text{(Sub-domain III)} \quad (25)$$

where $C_{O_2,N}$ and $C_{O_2,agg}$ represent, respectively, the concentration of oxygen in the Nafion coating and in the agglomerate. $D_{O_2,agg}^{eff}$ is the effective diffusion coefficient of oxygen in the agglomerate and k_v is the volumetric reaction rate constant in the agglomerate. The detailed derivation of Eqs. (23)–(25) is enclosed in Appendix A. The correction factor ξ_{O_2} can be obtained by solving Eqs. (23)–(25). The expression of the correction factor and related correlations in detail are listed in Table 1.

2.6. Current balance and cell voltage

In a working fuel cell, which is part of the circuit, the mean current densities at the anode and cathode can be respectively calculated by:

$$I_a = \frac{\int\int_{ACL} i_a\,dx\,dy}{h_c + h_r} \quad (26)$$

Table 1
Expressions of correction factor and related correlations for the agglomerate model

Descriptions	Expressions
Total correction factor	$\xi_{O_2} = \frac{1}{k_H}\xi_N\xi_{agg}$
Correction factor for Nafion coating	$\xi_N = \frac{1}{1+(2/3)(D_{agg}^{eff}/D_N)(\phi_s\coth\phi_s - 1)\ln(R_{agg}+\delta_N)/R_{agg}}$
Correction factor for agglomerate	$\xi_{agg} = \frac{6R_{in}^2}{R_{agg}\phi_s}\frac{I'(\phi_s)}{I(\phi_s)}f(\theta)$
The Thiele modulus	$\phi_s = R_{in}\sqrt{k_v/D_{O_2,agg}^{eff}}$
The volume reaction rate constant	$k_v = \sqrt{\frac{A_c i_{O_2}^{ref}}{4F(1-\varepsilon_{cc})D_{O_2,agg}^{eff}C_{O_2}^{ref}}}\exp\left[\frac{\alpha_c F}{2RT}(\varphi_m-\varphi_c)\right]$
Function related to overlapping angle	$f(\theta) = \frac{\cos\theta}{[2-(1-\cos\theta)^2(2+\cos\theta)]}$
Function related to the Thiele modulus	$I(\phi_s) = \sum_{n=0}^{\infty}[C_n'(R_{agg}-R_{in})^n]$

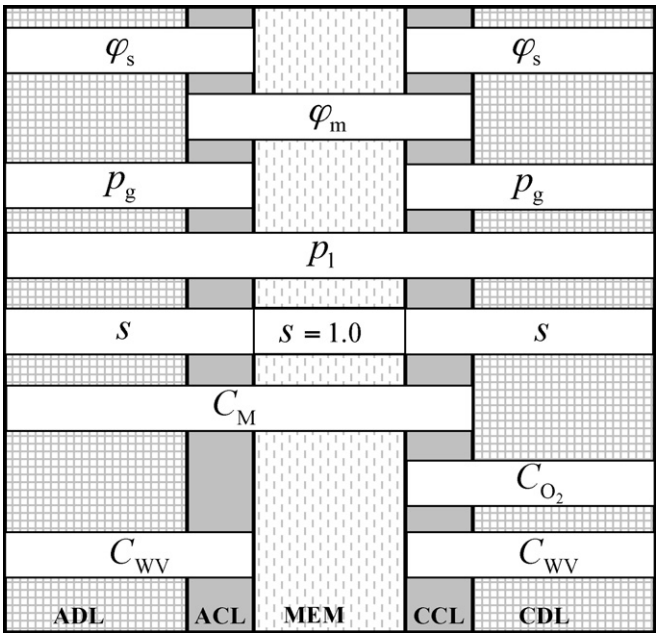

Fig. 3. Specified computational sub-domains for the solving variables.

$$I_c = \frac{\int\int_{CCL} i_c \, dx \, dy}{h_c + h_r} \tag{27}$$

Because part of the oxygen is consumed by the MDOR in the CCL, the current conservation equation can be expressed as:

$$I_{Cell} = I_a = I_c - I_p \tag{28}$$

where the 'parasitic' current, I_p, is a virtual current and denotes the fuel loss caused by methanol crossover. It is worth to point out that, unlike the assumptions adopted by many other literatures that the 'parasitic' current is distributed uniformly on the x direction in the CCL, the 'parasitic' current in this model is calculated by adopting a Tafel-like expression similar to that used in literature [6].

$$i_p = A_c i_M^{ref} \left(\frac{C_M \xi_M}{C_M^{ref}} \right)^{\gamma} \exp\left[\frac{\alpha_a F}{RT} (\varphi_{m,c} - \varphi_{s,c}) \right] \tag{29}$$

Finally, the cell voltage can be determined from the expression as follows:

$$V_{Cell} = V_0 - \varphi_{s,a}^0 \tag{30}$$

where V_0 is the thermodynamic equilibrium voltage of a DMFC; $\varphi_{s,a}^0$ represents the virtual local potential on the ribs of the anode flow-field plate. Note that the electric resistance in the electrolyte phase is implicitly accounted by the potential drop in the electrolyte-phase-region when solving the potential governing equations.

Up to this point, all the governing equations related to the two-phase mass transport and electrochemical reactions have been presented. In order to exhibit the detailed information of the governing equations, the computational sub-domains for solving variables are shown in Fig. 3. The expressions of source terms of the specific equations and correlations of several coefficients are listed in Table 2.

2.7. Boundary conditions

Boundary conditions are necessary for each governing equation restricted to the corresponding computational sub-domains. Conditions at different boundaries marked with Arabic number symbols are given as follows:

(I) *Boundaries 1 and 3*: These two boundaries are the interfaces between the ADL and the ribs of the anode flow-field plate. These interfaces are impermeable for reactants but permeable for electrons:

$$\frac{\partial p_l}{\partial x} = 0, \quad \frac{\partial p_g}{\partial x} = 0, \quad \frac{\partial s}{\partial x} = 0, \quad \frac{\partial C_M}{\partial x} = 0,$$
$$\frac{\partial C_{WV}}{\partial x} = 0, \quad \varphi_s = \varphi_{s,a}^0 \tag{31}$$

(II) *Boundary 2*: This boundary is the interface between the ADL and the AFC, which is the inlet of methanol solution and outlet of carbon dioxide and water vapor. This boundary is impermeable for the electrons:

$$p_l = p_{l,a}^{in}, \quad p_g = p_{l,a}^{in} + p_{c,a}^{channel}, \quad s = s_a^{channel},$$
$$C_M = C_M^{in}, \quad C_{WV} = C_{WV}^{sat}, \quad \frac{\partial \varphi_s}{\partial x} = 0 \tag{32}$$

(III) *Boundaries 4 and 8*: The symmetrical conditions for all variables are specified at these two boundaries as the computational domain is a periodic unit of the entire cell:

$$\frac{\partial p_l}{\partial y} = 0, \quad \frac{\partial p_g}{\partial y} = 0, \quad \frac{\partial s}{\partial y} = 0, \quad \frac{\partial C_M}{\partial y} = 0,$$
$$\frac{\partial C_{WV}}{\partial y} = 0, \quad \frac{\partial C_{O_2}}{\partial y} = 0, \quad \frac{\partial \varphi_s}{\partial y} = 0, \quad \frac{\partial \varphi_m}{\partial y} = 0 \tag{33}$$

(IV) *Boundaries 5 and 7*: These two boundaries are the interfaces between the DL and ribs at the cathode side. Similar to boundaries 1 and 3, the conditions at these two boundaries can be given as:

$$\frac{\partial p_l}{\partial x} = 0, \quad \frac{\partial p_g}{\partial x} = 0, \quad \frac{\partial s}{\partial x} = 0, \quad \frac{\partial C_{O_2}}{\partial x} = 0,$$
$$\frac{\partial C_{WV}}{\partial x} = 0, \quad \varphi_s = 0 \tag{34}$$

(V) *Boundary 6*: Similar to boundary 2, this boundary represents the inlet of reactants on the cathode side. The following boundary conditions at this interface are specified:

$$p_l = p_{g,c}^{in} + p_c^{channel}, \quad p_g = p_{g,c}^{in}, \quad s = s_c^{channel},$$
$$C_{O_2} = C_{O_2}^{in}, C_{WV} = 0, \quad \frac{\partial \varphi_s}{\partial x} = 0 \tag{35}$$

(VI) *Boundaries 9 and 12*: As the left and right boundaries of the electrolyte-phase-region, which are impermeable walls for protons. Accordingly, the flux of protons is zero at these two boundaries:

$$N_{H^+} = 0 \tag{36}$$

where N_{H^+} represents the molar flux of protons.

(VII) *Boundary 10*: This boundary is the interface between the ACL and MEM. As the membrane is treated as an impermeable wall for the electrons and gas phase, the conditions at this interface can be given as:

$$N_{e^-} = 0, \quad N_{WV} = 0 \tag{37}$$

(VIII) *Boundary 11*: Similar to boundary 10, conditions for this interface can be specified as:

$$N_{e^-} = 0, \quad N_{WV} = 0, \quad N_{O_2} = 0 \tag{38}$$

The liquid saturation at boundary 2, $s_a^{channel}$, is one of the key parameters in the present model. $s_a^{channel}$ depends strongly on both mass transport through the AFC/ADL interface and the complicated two-phase flow in the AFC. It is a rather challenging work to

Table 2
Expressions of source terms and coefficients of the governing equations

Parameters, symbols	Expressions in sub-domains of computational			
	ADL	ACL	CCL	CDL
Generation rate of protons, i_m	0	i_a	$i_c - i_p$	0
Generation rate of electrons, i_s	0	$-i_a$	$-(i_c - i_p)$	0
Generation rate of mass in gas phase, $\dot{m}_g$	$M_W\dot{R}_W$	$M_W\dot{R}_W + M_{CO_2}\dot{R}_{CO_2}$	$M_W\dot{R}_W + M_{CO_2}\dot{R}_{CO_2} + M_{O_2}\dot{R}_{O_2}$	$M_W\dot{R}_W$
Generation rate of mass in liquid phase, $\dot{m}_l$	$-M_W\dot{R}_W$	$-M_W\dot{R}_W - M_{CO_2}\dot{R}_{CO_2}$	$-M_W\dot{R}_W - M_{CO_2}\dot{R}_{CO_2} - M_{O_2}\dot{R}_{O_2}$	$-M_W\dot{R}_W$
Mole generation rate of species				
$\dot{R}_M$	0	$-i_a/(6F)$	$-i_p/(6F)$	0
$\dot{R}_{O_2}$	0	0	$-i_c/(4F)$	0
$\dot{R}_{WV}$	$\dot{R}_W$	$\dot{R}_W$	$\dot{R}_W$	$\dot{R}_W$
$\dot{R}_{CO_2}$	0	$i_a/(6F)$	$i_p/(6F)$	0
Interfacial molar transfer rate of water between liquid and vapor [38], $\dot{R}_W$	$k_e\frac{\varepsilon s\rho_l}{2M_W}(p_W^{sat} - y_{WV}p_g)q + k_c\frac{\varepsilon(1-s)y_{WV}}{2RT}(p_W^{sat} - y_{WV}p_g)(1-q)$			
Switch factor	$q = \left(1 + \frac{p_W^{sat} - y_{WV}p_g}{\lvert p_W^{sat} - y_{WV}p_g\rvert}\right)$			
Effective diffusion coefficients of methanol	$D_M^{eff} = D_{M,l}(\varepsilon s)^{1.5}$			
Effective diffusion coefficients of species in gas phase	$D_i^{eff} = D_{i,g}\left[\frac{\varepsilon(1-s)-\varepsilon_0}{1-\varepsilon_0}\right]^2$			

model the mass transport in liquid–gas two-phase flow in the AFC. Additionally, the AFC is perpendicular to and not involved in the computational domain, so some simplifications are necessary. In this situation, many researchers prefer to specify the liquid saturation in the AFC as a constant [17,18]. In order to reflect the saturation level in the AFC for various cell current density, the average of liquid saturation at the inlet and outlet of the AFC is applied in the present model instead of a specified value. The mass conservation equation in the AFC can be given as:

$$\frac{Q_a^{in}}{A} - u_{l,a}^{outlet}s_a^{outlet} = V_{l,afc} \tag{39}$$

$$u_{g,a}^{outlet}(1 - s_a^{outlet}) = V_{g,afc} \tag{40}$$

where $u_{l,a}^{outlet}$, $u_{g,a}^{outlet}$ and s_a^{outlet} represent the liquid velocity, gas velocity and liquid saturation at the outlet of the AFC. Q_a^{in} is the volumetric flow rate of methanol solution at the anode inlet. A is the area of the cross-section of the AFC. $V_{1,afc}$ and $V_{g,afc}$ stand for volumetric flow rates of liquid and gas phases at the AFC/ADL interface. According to the present visualization research [21], the slug flow rather than the bubble flow is more frequently encountered in the AFC. In the slug flow, the large difference between gas velocity and liquid velocity has significant influences on the mass transport in the AFC. For more realistic modeling of the AFC, instead of the homogeneous model, a simplified expression derived from the drift-flux models [35,36] is applied to describe the relationship between the gas velocity and liquid velocity:

$$u_{g,a}^{outlet} = 1.35\left[(1 - s_a^{outlet})u_{g,a}^{outlet} + s_a^{outlet}u_{l,a}^{outlet}\right] \tag{41}$$

By solving Eqs. (39)–(41), we can obtain s_a^{outlet}. And then $s_a^{channel}$ can be calculated from the expression below:

$$s_a^{channel} = \frac{1 + s_a^{outlet}}{2} \tag{42}$$

3. Numerical results and discussion

A self-written code based on the finite-volume-method is developed to solve the governing equations iteratively under the baseline conditions and parameters given in Tables 3 and 4. Model validation and the distributions of several variable fields are present below.

3.1. Model validation

Cell performance predicted by the present model for the DMFC fed with 0.25 M and 0.5 M methanol solution is compared with the experimental data [37] in Fig. 4 under the same operation conditions, including the anode flow rate of 1.0 ml min^{-1} for 15 channels, the cathode flow rate of 1000 ml min^{-1} and the cell temperature at 75 °C. In order to validate the reliability of the present model, the same set of parameters are used to predict the polarization behavior for different methanol feeding concentrations. As can be seen from Fig. 4, the predicted polarization curves are generally in good agreement with the experimental data. The deviations of the predicted data from the experimental data in the low current density region are probably caused by the simplifications used in the modeling of the two-phase flow in the AFC. It can also be found from the power density curves that the highest power density is achieved at the front-end of the concentration polarization region, so it is a wise choice to let the DMFC work in the Ohm polarization region.

3.2. Mechanism analysis of species transport

The transport processes of species in a DMFC are very complicated as they are intrinsically coupled with both the elec-

Table 3
Geometric and operating parameters of the DMFC

Parameters	Symbols	Value	Unit
Structure parameters			
Porosity, thickness			
ADL	ε_{adl}, l_{adl}	0.64, 2.6×10^{-4}	–, m
ACL	ε_{acl}, l_{acl}	0.3, 0.2×10^{-4}	–, m
MEM	ε_{mem}, l_{mem}	0.3, 1.3×10^{-4}	–, m
CCL	ε_{ccl}, l_{ccl}	0.3, 0.2×10^{-4}	–, m
CDL	ε_{cdl}, l_{cdl}	0.64, 2.6×10^{-4}	–, m
Height of a half rib	h_r	0.5×10^{-3}	m
Height of channels	h_c	1×10^{-3}	m
Length of channels	L_c	3×10^{-2}	m
Operation conditions			
Operation temperature	T	348.15	K
Anode channel inlet pressure	$p_{l,a}^{in}$	101325	Pa
Cathode channel inlet pressure	$p_{g,c}^{in}$	101325	Pa
Anode flow rate	$Q_{a,in}$	1	ml min^{-1}
Inlet methanol concentration at anode	C_M^{in}	250-500	mol m^{-3}
Inlet oxygen concentration at cathode	$C_{O_2}^{in}$	35	mol m^{-3}

Table 4
Physicochemical properties and electrochemical kinetics parameters used in simulation

Parameters	Symbols	Value	Unit	References
Physicochemical properties				
Nafion volume fraction in ACL and CCL	$\varepsilon_{N,acl}$, $\varepsilon_{N,ccl}$	0.4, 0.4		
Conductivity in membrane phase	σ_m	$7.3e^{[1268(1/298-1/T)]}$	$\Omega^{-1}\,m^{-1}$	[3]
Conductivity in solid phase	σ_s	1.2×10^{4}	$\Omega^{-1}\,m^{-1}$	
Permeability				
ADL	K_{adl}	2×10^{-12}	m^2	[15]
ACL	K_{acl}	1×10^{-14}	m^2	[15]
MEM	K_{mem}	5×10^{-18}	m^2	
CCL	K_{ccl}	1×10^{-14}	m^2	[15]
CDL	K_{cdl}	2×10^{-12}	m^2	[15]
Viscosity of gas phase	μ_g	2.03×10^{-5}	$kg\,m^{-1}\,s^{-1}$	[38]
Viscosity of liquid phase	μ_l	4.06×10^{-4}	$kg\,m^{-1}\,s^{-1}$	[15]
Electro-osmotic coefficients of water	n_d	2.5		[17]
Diffusivities				
Methanol in liquid water	$D_{M,l}$	$10^{-5.4163-999.778/T}$	$m^2\,s^{-1}$	[12]
Methanol in Nafion	$D_{M,N}$	$4.9\times10^{-10}e^{[2436(1/333-1/T)]}$	$m^2\,s^{-1}$	[3]
Oxygen in gas phase	$D_{O_2,g}$	$1.775\times10^{-5}(T/273.15)^{1.823}$	$m^2\,s^{-1}$	[12]
Oxygen in Nafion	$D_{O_2,N}$	1.844×10^{-10}	$m^2\,s^{-1}$	[39]
Vapor in gas	$D_{WV,g}$	$2.56\times10^{-5}(T/307.15)^{2.334}$	$m^2\,s^{-1}$	[12]
Henry law constant	k_H	$0.3125\times101325/(RT)$ $-2.1794+0.02953\,(T-273)$		[27]
Saturation pressure of vapor	$\log_{10} p_W^{sat}$	$-9.1837\times10^{-5}\,(T-273)^2$ $+1.4454\times10^{-7}\,(T-273)^3$	atm	[15]
Evaporation rate constant of water	k_e	5×10^{-3}	$atm^{-1}\,s^{-1}$	[40]
Condensation rate constant of water	k_c	50	s^{-1}	[40]
Electrochemical kinetics parameters				
Exchange current density				
Anode	$A_a i_M^{ref}$	5.8×10^{4}	$A\,m^{-3}$	
Cathode	$A_c i_{O_2}^{ref}$	2.35×10^{2}	$A\,m^{-3}$	
Methanol crossover	$A_c i_M^{ref}$	1×10^{5}	$A\,m^{-3}$	
Reference concentration of methanol	C_M^{ref}	100	$mol\,m^{-3}$	[12]
Reference concentration of oxygen	$C_{O_2}^{ref}$	0.52	$mol\,m^{-3}$	[15]
Transfer coefficient of anode	α_a	0.5		[40]
Transfer coefficient of cathode	α_c	1.0		[15]
Thermodynamic voltage	V_0	1.21	V	[12]

trochemical reactions and the mass transport between liquid and gas phases. So better understanding of fundamental species transport mechanisms in a DMFC is essential to the optimization of the cell design.

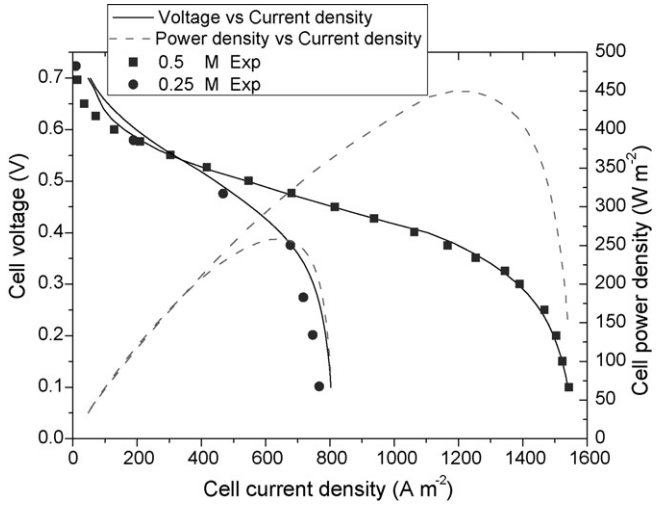

Fig. 4. Comparison of cell performance predicted by the present model and experimental data [37].

The concentration distributions of methanol and oxygen are given in Fig. 5(a) and (b) respectively. A sharp decrease in methanol concentration can be seen from the AFC to the ACL due to the consumption in the MOR. The methanol concentration also decreases from the under-channel region to the under-rib region because ribs of the flow-field plate limit the access of methanol solution to the ACL. As a contrast, the distribution of oxygen concentration in the CDL and CCL is nearly uniform, which can be observed from Fig. 5(b). The largest relative difference of oxygen concentration is 0.63%. This is because the diffusion coefficient of oxygen is several orders of magnitude higher than that of methanol and the density of the gas phase is very low. Fig. 5 indicates that the degradation of cell performance caused by the concentration polarization on the electrodes is mainly due to the mass transport limitation of methanol. In section 3.4, the non-uniform distribution of MOR rate mainly caused by the non-uniform distribution of methanol concentration in the ACL will also be observed.

The total flux of methanol transport consists of two contributions with different transport mechanisms: diffusion caused by the gradient of methanol concentration as can be seen from Fig. 5(a) and convection caused by the bulk motion of the liquid phase. The liquid motion in the MEA is driven by the gradient of liquid pressure and the electro-osmotic drag force. Noteworthy is that most of the previous models for DMFCs mainly focus on the transport phenomena in the anodic or cathodic porous media. The present model also provides a modeling of the simultaneous methanol and water transport across the MEM. Fig. 6 shows the distributions of

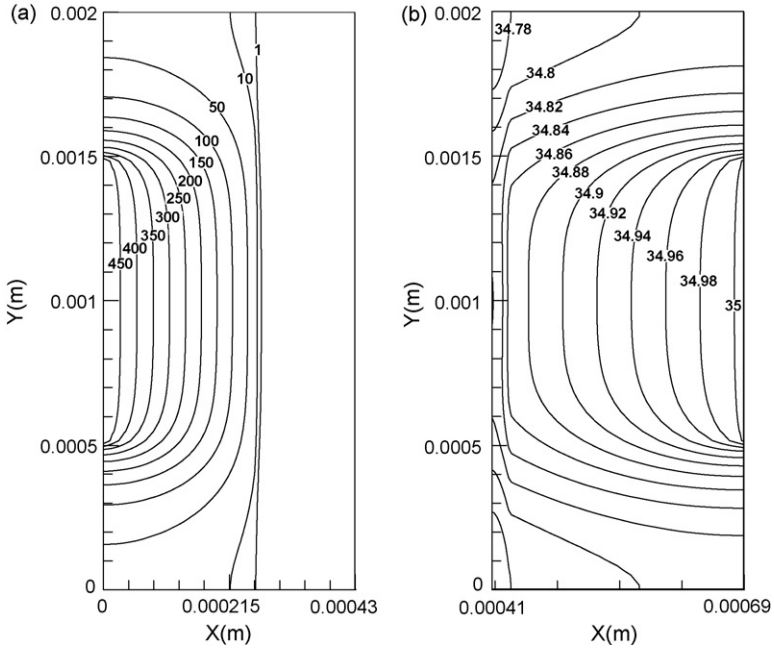

Fig. 5. Distribution of (a) methanol concentration in four layers: ADL, ACL, MEM and CCL, (b) oxygen concentration in the cathode (Cell voltage: 0.11 V).

velocity fields of liquid and gas phases in the upper half of the computational domain. Apparently, the complex liquid–gas two-phase counter-flow behaviour can be seen in the porous MEA. As shown in Fig. 6(a), the methanol solution moves from the AFC to the ACL in two directions: directly to the under-channel region of the ACL and snaking through the ADL to the under-rib region of the ACL. And then, the excess water and methanol in the ACL permeate through the MEM to the CCL, where methanol is totally oxidized and the ORR takes place to form water. The produced water, along with the water crossing over from the anode, transfers through the CDL to the CFC. By contrast, the gas phase movement in the opposite direction can be seen from Fig. 6(b), as oxygen is consumed in the CCL while carbon dioxide is simultaneously generated in the ACL. Because the MEM is regarded as a gas insulator, there is a blank of the gas velocity field in this region.

In order to quantify the effects of diffusion and convection on the methanol transport in the ACL, their contributions to the mean current density for 0.25 M and 0.5 M methanol feeding concentrations are compared in Fig. 7. It can be clearly seen that convection only accounts for a small fraction of the total flux of methanol. More than

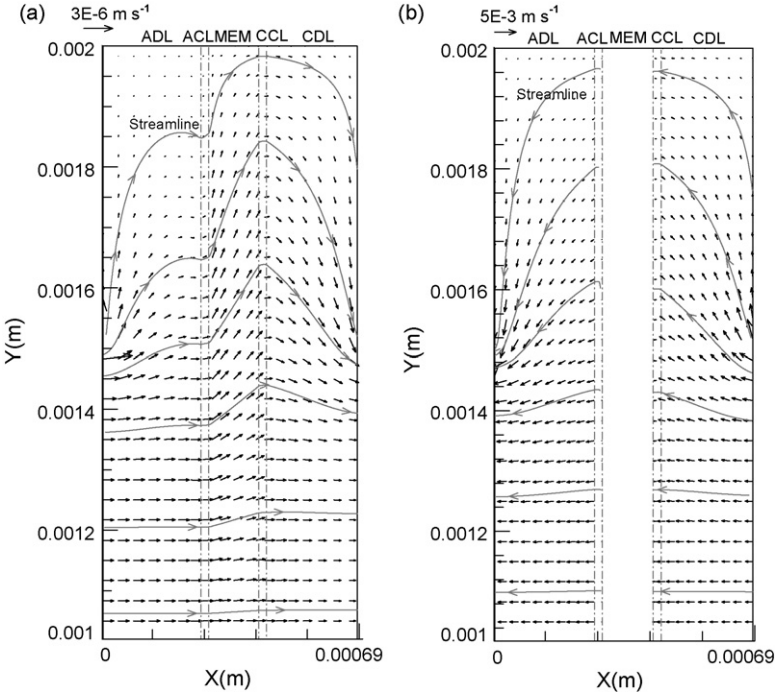

Fig. 6. Distribution of velocity vector of (a) liquid phase and (b) gas phase in the upper half of the computational domain (Cell voltage: 0.11 V).

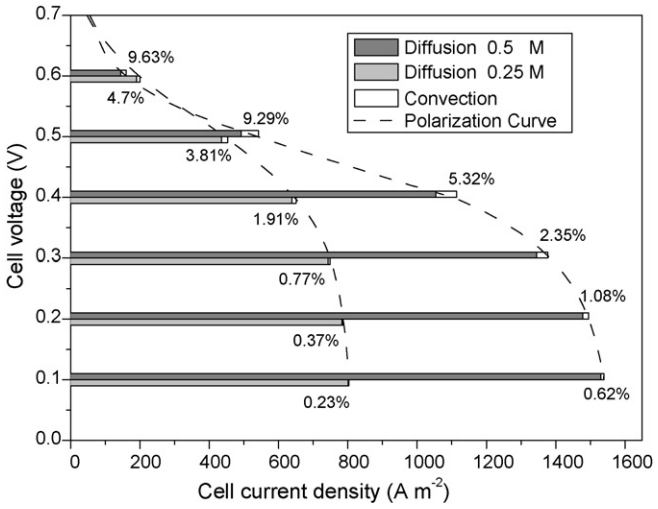

Fig. 7. Share of contributions of diffusive and convective transport to the cell current density for various cell voltage.

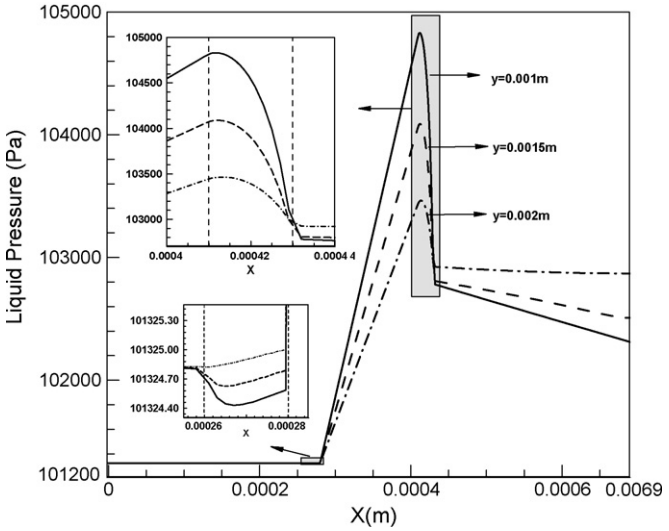

Fig. 8. Liquid pressure along *x* direction for different locations on *y* direction (Cell voltage: 0.11 V).

90% of the mean current density results from methanol diffusive transport, which indicates that the mass transport of methanol in the ACL is dominated by diffusion mechanism. Besides that, another trend can be observed that the percentage of convection for a given methanol feeding concentration, 0.25 M or 0.5 M, decreases with an increase in cell current density. This phenomena result from the combined effects of liquid velocity and methanol concentration on methanol transport. When the current density becomes larger, more methanol and water will be consumed in the ACL, and this will lead to an increase in the liquid velocity and a decrease in the methanol concentration. Accordingly, it is easy to conceive that the contribution of the increased liquid velocity to the methanol convection is weakened or even submerged by the decreased methanol concentration while the diffusive transport contributes more significantly to the total methanol flux due to the increase in the concentration gradient of methanol. According to the above analysis, it can be seen that convection is a weak point in methanol transport processes. Efforts on enhancing the convective methanol transport can significantly improve the cell performance.

3.3. Analysis of water and methanol crossovers through the MEM

Water and methanol crossovers through the MEM from the anode to the cathode are two of the key technological challenges in the research of DMFCs. The total flux of methanol crossover is comprised of three contributions, namely: diffusion due to the concentration gradient of methanol, back convection due to the bulk motion under adverse pressure gradient and electro-osmotic drag flow due to the transport of protons in the electrolyte phase. As it is assumed that the MEM is fully hydrated and no water diffusion occurs, water crossover mainly rests with the back convection and electro-osmotic drag flow.

Fig. 8 shows the liquid pressure profiles along *x* direction of the computational domain at three different locations on *y* direction. It can be seen that the liquid pressure increases rapidly in the MEM. This huge adverse pressure gradient causes the back convection of methanol solution from the cathode to the anode, which can reduce methanol crossover, and is beneficial to the cell performance. In this model, we considered the contribution of electro-osmotic drag to liquid velocity not only in the MEM but also in CLs. It can be observed from the detailed view of the liquid pressure profiles that the driving force of liquid velocity is transferred gradually from pressure gradient to electro-osmotic drag force, exhibited as the minimum and maximum points of the liquid pressure profiles. This proves that it is necessary to consider the electro-osmotic drag flow in CLs in order to avoid the overestimate of the contribution of pressure gradient to the liquid velocity, especially on the cathode side. Also in Fig. 8, the liquid pressure in the under-rib region of the CDL is higher than that in the under-channel region. This trend agrees well with the results reported in [15,17] as the liquid water is prone to accumulate in the corner under ribs. However, a higher and sharply decreasing liquid pressure in the under-channel region in the CCL can also be seen from the detailed view of liquid pressure in the CCL. This pressure profile indicates that the water flux in the under-channel region of the CCL is heavier than that in the under-rib region. The water flux in the CCL includes water generated by

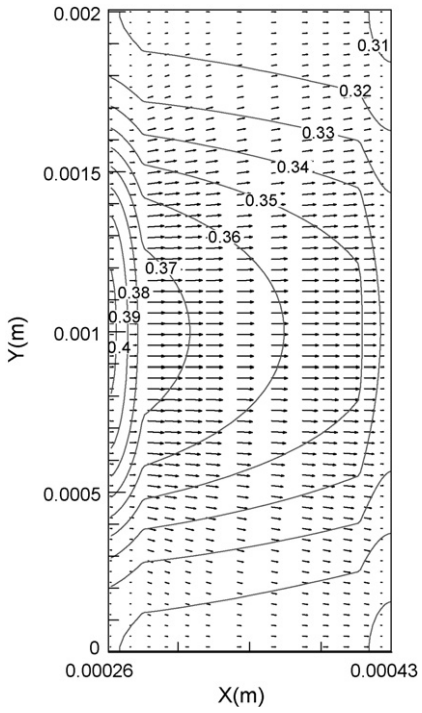

Fig. 9. Distribution of potential of electrolyte phase and the local current of protons in the electrolyte-phase-region (Cell voltage: 0.11 V).

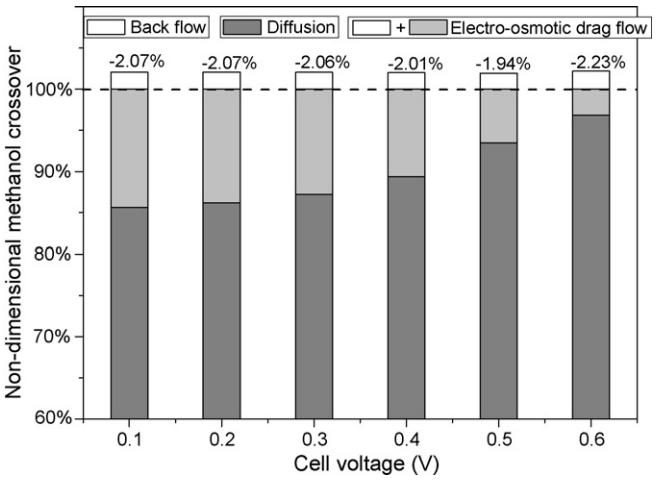

Fig. 10. Percentage of contributions resulting from different methanol transport mechanisms to the total methanol crossover flux for various cell voltage.

the ORR and more importantly, flux of water crossover through the MEM, which is the larger part of the total water amount.

The distributions of potential and the local current of protons in electrolyte-phase-region are shown in Fig. 9. Similar to the distribution of methanol concentration, the electrolyte phase potential decreases from the ACL to the CCL and from the under-channel region to the under-rib region. This is a result of the higher proton generation rate in the under-channel region of the ACL as protons move from the ACL to the CCL driven by the electrical field force. The generation and consumption of protons in terms of the increase and decrease in the local current vector can also be observed from the sub-regions: $x = 0.00026–0.00028$ m and $x = 0.00041–0.00043$ m.

Figs. 8 and 9 provide a detailed description of water crossover through the MEM. A common feature of these two figures is that both the liquid pressure gradient and electro-osmotic drag force promote the migration of protons, methanol and water from the under-channel region to the under-rib region in the electrolyte-phase-region, which can also be clearly seen in Fig. 6(a). This migration process can reduce the non-uniformity of the DMFC, make better usage of the catalyst in the CCL and thus is beneficial to the cell performance.

In order to graphically show the effects of each methanol transport mechanism on the methanol crossover, the percentage of their contributions to the total flux of methanol crossover are calculated. As can be seen in Fig. 10, the scale of the percentage is set to begin with 60% to give prominence to the difference between cases for various cell voltages. Clearly, the diffusive transport dominates methanol crossover with a share of more than 85%. The back convection of methanol solution can reduce methanol crossover flux by approximately 2%. So carefully adjusting the inlet pressure of the AFC and CFC or making some structure improvements, such as adding a micro-pore layer between the CCL and CDL will suppress methanol crossover by increasing the back convection flux of methanol solution.

3.4. Analysis of the distributions of electrochemical reaction rates in CLs

Electrochemical reactions occurring in CLs of the DMFC are very complicated multi-step processes which are always described by empirical expressions like Eqs. (19) and (20). Because the overpotential is at the power position of the Euler's constant (approximately 2.7183), it has significant impact on the electrochemical reaction rates. In the present model, we calculated the

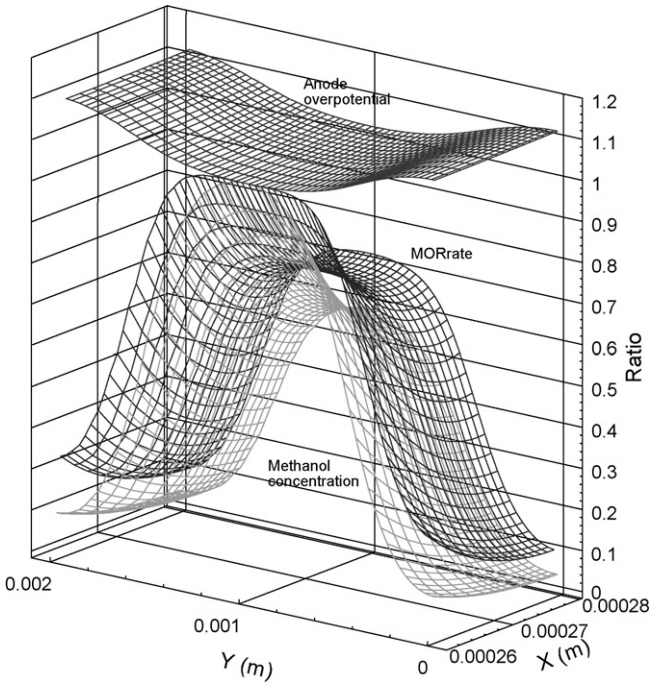

Fig. 11. Distribution of overpotential, MOR rate and methanol concentration in the ACL (Cell voltage: 0.31 V).

distribution of overpotential and the effect of overpotential on electrochemical reaction rates, as shown in Figs. 11–13. It should be noted that the non-dimensional relative scale is adopted for the investigated variables to clearly show their distributions because the methanol concentration and electrochemical reaction rates vary within several orders of magnitude. Values of variables at point ($x = 0.00026$ m, $y = 0.001$ m) are set as the reference values in the ACL, and values of variables at point ($x = 0.00041$ m, $y = 0.001$ m) are set as the reference values in the CCL.

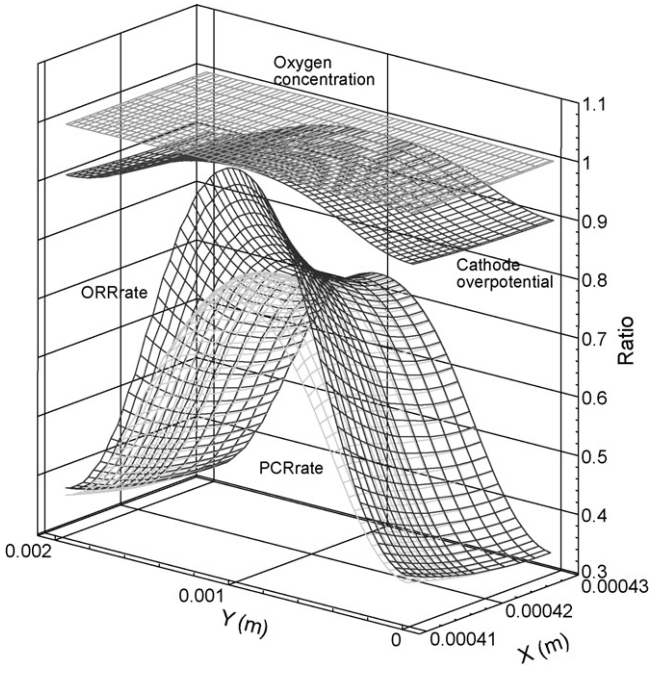

Fig. 12. Distribution of oxygen concentration, overpotential, ORR rate and PCR rate in the CCL (Cell voltage: 0.31 V).

The distributions of anode overpotential, MOR rate and methanol concentration in the ACL are presented in Fig. 11. Apparently, methanol concentration decreases sharply from the under-channel region to the under-rib region and gently along x direction, while the distribution of anode overpotential displays a reverse but more gradual trend. As a result of the combined effects of methanol concentration and anode overpotential, the distribution of MOR rate appears in the shape of a saddle, similar to the distribution of methanol concentration but having an uprising in the region close to the MEM. So it can be concluded that the MOR rate in the ACL is mainly dominated by the methanol concentration while the work point of the cell is within the mass transport controlled region. Also in Fig. 11, the anode overpotential exhibits a self-regulation characterize to the effect of non-uniform distribution of methanol concentration on the MOR rate by making the distribution of MOR rate more uniform throughout the ACL.

It has been mentioned about the results in Fig. 5 that the distribution of oxygen concentration in the CCL is almost uniform, which can also be seen in Fig. 12. If the overpotential in the CCL is set as a constant, the uniform distribution of ORR rate will be expected logically. However, an extremely non-uniform distribution of ORR rate can be seen in Fig. 12 due to the slightly decrease in the cathode overpotential in the under-rib region. These distributions indicate that the non-uniformity of the ORR rate in the CCL depends highly on the cathode overpotential. As mentioned above, the total amount of oxygen consumed in the ORR includes two parts: oxygen reacted with protons transported from the anode, named proton consumption reaction (PCR) in this paper, and oxygen consumed in the MDOR. In Fig. 12, a large gap between the PCR rate and the ORR rate in the region near the MEM can be observed, and this indicates that although most of the oxygen in the CCL is consumed in the region near the MEM, only part of the oxygen participates in the PCR. And this situation will get worse when the DMFC works at a lower current density as more methanol will permeate through the MEM. On the other hand, Fig. 12 also predicts a non-uniform distribution of the MDOR rate which can be clearly seen in Fig. 13. The distribution of methanol concentration in the CCL is extremely non-uniform and the MDOR rate decreases more sharply than methanol concentration along both x and y directions because of the effect of the slight non-uniform distribution of cathode overpotential. The results showed in Figs. 11–13 indicate that accounting for the simultaneous transport processes of protons, methanol and water in the electrolyte-phase-region is helpful in achieving a more realistic prediction of the distribution of electrochemical reaction rates in CLs.

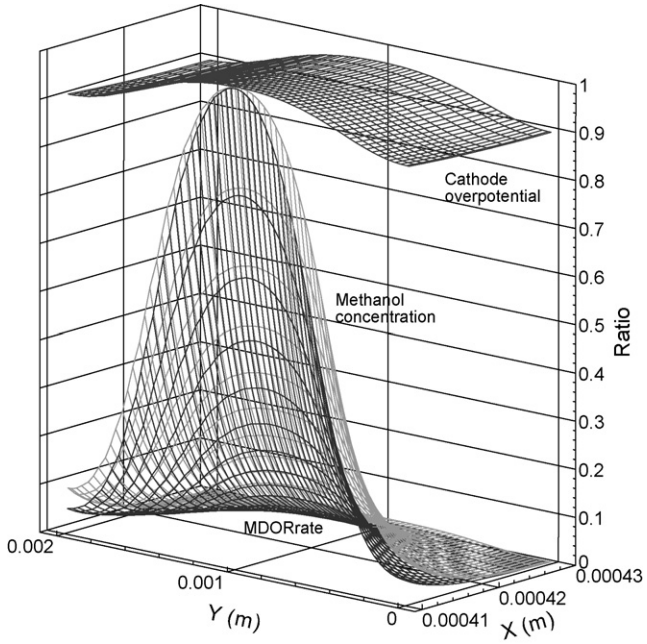

Fig. 13. Distribution of overpotential, methanol concentration and MDOR rate in the CCL (Cell voltage: 0.31 V).

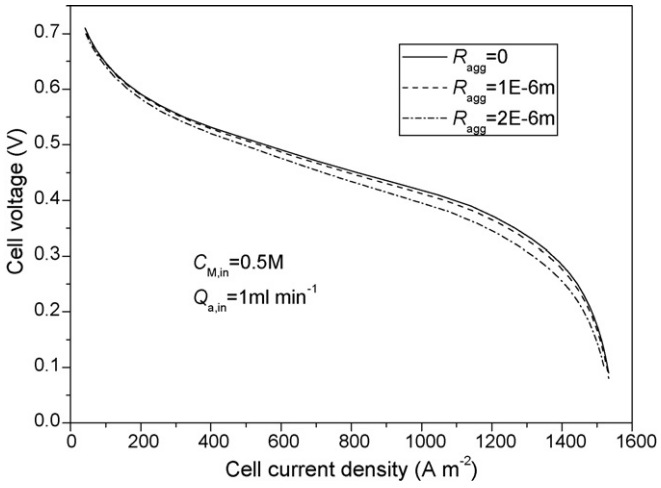

Fig. 14. Effect of the agglomerate radius on the cell performance.

3.5. Effect of the agglomerate radius and overlapping angle

A modified agglomerate model is introduced in this work to consider the effect of microstructure of the CLs on cell performance. Fig. 14 presents the effect of the agglomerate radius on polarization curves. The R_{agg} = 0 case corresponds to the homogeneous model in which the transport resistance in the agglomerates is not taken into account. It can be seen that the homogeneous model overestimates the cell performance due to neglect of the mass transfer resistance induced by agglomerates. Fig. 14 also shows that the cell voltage decreases with an increase in the agglomerate radius because of the higher mass transfer resistance

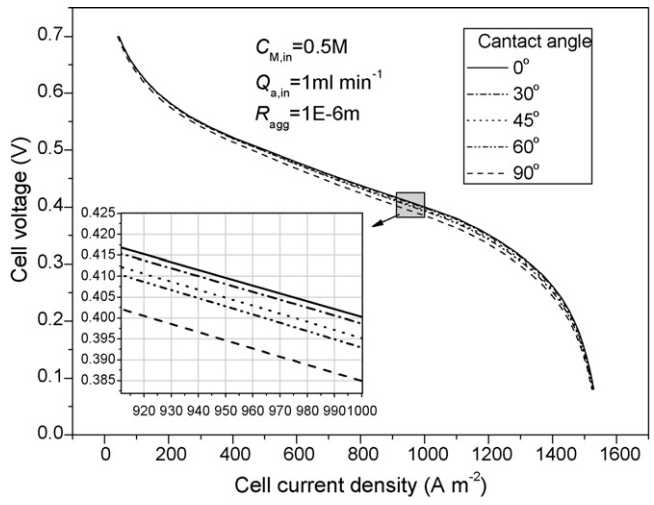

Fig. 15. Effect of the overlapping angle of agglomerates on the cell performance.

in larger agglomerate. Results in Fig. 14 indicate that fully dispersion of catalyst particles in the fabrication processes of the electrodes to achieve smaller size can lead to a better cell performance.

Besides that, the overlapping angle, another key parameter of the agglomerate, can reflect the topological of the agglomerates to a certain extent. The effect of the overlapping angle on cell performance is shown in Fig. 15. Note that agglomerates with overlapping angles equal to 0 and 90 degrees correspond to the spherical and cylindrical agglomerate geometry respectively. And our modified model can predict the general microstructure of agglomerate with an overlapping angle between 0 and 60 degrees. An increase in the overlapping angle only leads to a slight decrease in the cell voltage, implying that the overlapping angle in the present agglomerate model has a rather little effect on the polarization curve. This little effect is probably attributed to the decrease in the specific surface area of the agglomerates when the overlapping angle becomes larger.

4. Conclusions

A two-dimensional, two-phase mass transport model adopting a modified agglomerate model has been developed to investigate the mechanisms of species transport processes and the distributions of several key variables in the DMFC. The microstructure of the CLs and the effect of electro-osmotic drag on the liquid motion in the electrolyte-phase-region are considered. The electrons and protons transport processes are also taken into account to numerically calculate the distribution of overpotential in both ACL and CCL. Based on the analysis of the numerical results, conclusions are summarized as follows:

(1) The distribution of methanol concentration is significantly non-uniform along both x and y directions in the computational domain. As a contrast, almost uniform distribution of oxygen concentration appears in the cathodic porous region due to the lower transport resistance for gas phase in the CDL. Compared with convection, diffusive transport dominates the methanol transport and has major effect on the working current density.
(2) Methanol crossover mainly results from the diffusive transport while water crossover mainly rests with the electro-osmotic drag flow. In the electrolyte-phase-region, methanol and water is prone to transfer from the under-channel region to the under-rib region in addition to the main transport processes along x direction. Numerical results also show that it is necessary to consider the migration process of protons in the electrolyte phase to achieve a detailed description of the transport processes of protons, methanol and water throughout the electrolyte-phase-region.
(3) The distributions of different variables interact with each other and this convoluted relationship can be mainly understood as that non-uniform distribution of methanol concentration results in non-uniform distribution of MOR rate, and the latter will lead to a non-uniform distribution of overpotential in the CCL. An extremely non-uniform distribution of ORR rate appears in the CCL because of the significant effect of cathode overpotential on the ORR rate even though the distribution of oxygen is nearly uniform.
(4) The numerical results indicate that the modified agglomerate model in this paper can reflect a more reasonable and realistic microstructure of the CCL as well as the effect of this microstructure on the cell performance. The results also suggest that a smaller agglomerate size is beneficial to the cell performance.

Acknowledgements

This work is supported by the National Natural Science Fund for Distinguished Young Scholars from the National Natural Science Foundation of China (Nos. 50425620, 50629601) and the Key Project of National Natural Science Foundation of China (No.50736005).

Appendix A. Derivation of the correction factor ξ_{O_2} based on the modified agglomerate model

It can be seen from Fig. 2 that in order to supply access for the electrons, the neighboring agglomerates should share an overlapped region with each other. So a segmental spherical agglomerate geometry is adopted in this model with a simplification that only the transfer resistance on the radial direction is considered. The conservation equation of oxygen concentration in sub-domain I: the Nafion coating region, can be given as

$$\frac{R_{agg}\cos\theta}{r+dr}4\pi(r+dr)^2 D_N \frac{d}{dr}\left(C_{O_2,N}+\frac{dC_{O_2,N}}{dr}dr\right) - \frac{R_{agg}\cos\theta}{r}4\pi r^2 D_N \frac{dC_{O_2,N}}{dr}=0 \tag{A.1}$$

By simplifying Eq. (A.1), Eq. (23) can be obtained

$$\frac{d^2C_{O_2,N}}{dr^2}+\frac{1}{r}\frac{dC_{O_2,N}}{dr}=0 \tag{23}$$

In sub-domain II, the conservation equation can be written in the form similar to Eq. (23) with a non-zero source term:

$$\frac{d^2C_{O_2,agg}}{dr^2}+\frac{1}{r}\frac{dC_{O_2,agg}}{dr}=\frac{k_v}{D^{eff}_{O_2,agg}}C_{O_2,agg} \tag{24}$$

The geometry of sub-domain III is the same as the spherical agglomerate, so Eq. (25) with the same form as the standard concentration conservation equation in a spherical coordinate is suitable to formulate the mass transfer process in this region:

$$\frac{d^2C_{O_2,agg}}{dr^2}+\frac{2}{r}\frac{dC_{O_2,agg}}{dr}=\frac{k_v}{D^{eff}_{O_2,agg}}C_{O_2,agg} \tag{25}$$

Three variables: $C_{O_2,I}$, $C_{O_2,II}$ and $C_{O_2,III}$ are defined in this model to represent the oxygen concentration at the outer surfaces of sub-domains I–III. According to the spherical agglomerate model, we can obtain:

$$C_{O_2,agg}\big|_{r=R_{in}} = C_{O_2,I} \tag{A.2}$$

$$\left.\frac{dC_{O_2,agg}}{dr}\right|_{r=R_{in}} = \frac{C_{O_2,I}}{R_{in}}(\phi_s\coth\phi_s-1) \tag{A.3}$$

where the Thiele modulus is defined as

$$\phi_s = R_{in}\sqrt{k_v/D^{eff}_{O_2,agg}} \tag{A.4}$$

$$k_v = \sqrt{\frac{A_c i^{ref}_{O_2}}{4F(1-\varepsilon_{cc})D^{eff}_{O_2,agg}C^{ref}_{O_2}}}\exp\left[\frac{\alpha_c F}{2RT}(\varphi_m-\varphi_c)\right] \tag{A.5}$$

Eqs. (A.4) and (A.5) is used as the boundary condition of Eq. (24), which is a Bessel function and has a power series solution as follows:

$$C_{O_2,agg}(r) = C_{O_2,I}\sum_{n=0}^{\infty}C'_n(r-R_{in})^n \quad R_{in}\le r\le R_{agg} \tag{A.6}$$

where the coefficients can be given as

$$C'_0 = 1, \qquad C'_1 = \frac{1}{R_{in}}(\phi_s \coth \phi_s - 1) \tag{A.7}$$

$$C'_n = \frac{\sum_{k=0}^{n}[(k+1)a_{n-k}C'_{k+1}] + b_0 C'_k}{(n+1)(n+2)} \quad n = 0, 1, 2, \ldots \tag{A.8}$$

$$a_k = \frac{(-1)^k}{R_{in}^{k+1}} \quad k = 0, 1, 2, \ldots \tag{A.9}$$

$$b_0 = \left(\frac{\phi_s}{R_{in}}\right)^2 \tag{A.10}$$

The information at the outer interface of sub-domain II which can be obtained from Eq. (A.6) is as follows:

$$C_{O_2,II} = C_{O_2,agg}\big|_{r=R_{agg}} = C_{O_2,I}\sum_{n=0}^{\infty} C'_n (R_{agg} - R_{in})^n \tag{A.11}$$

$$\left.\frac{dC_{O_2,agg}}{dr}\right|_{r=R_{agg}} = C_{O_2,I}\sum_{n=1}^{\infty}[nC'_n(R_{agg} - R_{in})^{n-1}] \tag{A.12}$$

The correction factor ξ_{agg} in view of the transfer resistance in the agglomerate is defined as

$$\xi_{agg} = \frac{S_{agg} D^{eff}_{O_2,agg}(dC_{O_2,agg}/dr)\big|_{r=R_{agg}}}{V_{agg} k_v C_{O_2,II}} \tag{A.13}$$

where S_{agg} and V_{agg} represent the surface area and the volume of the agglomerate. By substituting Eqs. (A.11) and (A.12) into Eq. (A.13), the expression of ξ_{agg} is rewritten as

$$\xi_{agg} = \frac{6R_{in}^2}{R_{agg}\phi_s}\frac{I'(\phi_s)}{I(\phi_s)} f(\theta) \tag{A.14}$$

$$I(\phi_s) = \sum_{n=0}^{\infty}[C'_n(R_{agg} - R_{in})^n] \tag{A.15}$$

$$f(\theta) = \frac{\cos\theta}{[2 - (1 - \cos\theta)^2(2 + \cos\theta)]} \quad 0^\circ < \theta \le 60^\circ \tag{A.16}$$

For sub-domain I, the solution of Eq. (23) can be expressed as:

$$C_{O_2,N}(r) = a \ln r + b \tag{A.17}$$

where a and b are the coefficients related to the boundary conditions at the interface between sub-domains I and II and can be derived by considering Eqs. (A.11) and (A.12). So the correction factor ξ_N in view of the transfer resistance in the Nafion coating can be given as

$$\xi_N = \frac{1}{1 + (2/3)(D^{eff}_{agg}/D_N)(\phi_s \coth \phi_s - 1)\ln(R_{agg} + \delta_N)/R_{agg}} \tag{A.18}$$

Finally, the general correction factor ξ_{O_2} concerning the overall mass transport processes of oxygen from the gas pore to the active sites of catalyst particles can be calculated by the expression below:

$$\xi_{O_2} = \frac{1}{k_H}\xi_N \xi_{agg} \tag{A.19}$$

Appendix B. Nomenclature

List of symbols

A	specific area in the catalyst layer ($m^2\ m^{-3}$)
C	concentration ($mol\ m^{-3}$)
D	diffusivity ($m^2\ s^{-1}$)
F	Faraday constant (96485 $C\ mol^{-1}$)
h	height of channel or rib (m)
i	electrochemical reaction rate ($A\ m^{-3}$)
I	current density ($A\ m^{-2}$)
$\mathbf{I}$	current vector ($A\ m^{-2}$)
k_c	condensation rate of water (s^{-1})
k_e	evaporation rate of water ($atm^{-1}\ s^{-1}$)
k_H	Henry's law constant
k_{rg}	relative permeability of gas phase
k_{rl}	relative permeability of liquid phase
K	absolute permeability of porous media (m^2)
L	length of the channel (m)
$\dot{m}$	source terms in mass conservation equations ($kg\ m^{-3}\ s^{-1}$)
M	molecular weight ($kg\ mol^{-1}$)
n_d	electro-osmotic drag coefficient
N	molar flux ($mol\ m^2\ s^{-1}$)
p	pressure (Pa)
p_c	capillary pressure (Pa)
q	switch factor
Q	volume flow rate ($ml\ min^{-1}$)
R	gas constant ($J\ mol^{-1}\ K^{-1}$)
$\dot{R}$	source term in species conservation equations ($mol\ m^{-3}\ s^{-1}$)
R_W	interfacial transfer rate of water ($mol\ m^{-3}\ s^{-1}$)
s	liquid saturation
T	temperature (K)
$\mathbf{u}$	superficial velocity vector ($m\ s^{-1}$)
V_0	thermodynamic equilibrium voltage (V)
V_{cell}	cell voltage (V)

Greek symbols

α	transfer coefficient
γ	reaction order
δ_N	thickness of Nafion coating (m)
ε	porosity of the porous media
κ	conductivity of membrane phase ($\Omega^{-1}\ m^{-1}$)
μ	viscosity ($kg\ m^{-1}\ s^{-1}$)
θ	overlapping angle (°)
θ_c	contact angle (°)
ρ	density ($kg\ m^{-3}$)
σ	interfacial tension ($N\ m^{-1}$)

Superscripts

channel	the flow channel
eff	effective value
in	inlet of the flow channel
ref	reference value
sat	saturated

Subscripts

a	anode
acl	anode catalyst layer
adl	anode diffusion layer
agg	the agglomerate
c	cathode
ccl	cathode catalyst layer
cdl	cathode diffusion layer
e^-	electrons
g	gas phase
H^+	protons
in	the inner sphere
l	liquid phase
m	the membrane phase
mem	membrane
N	Nafion phase
O_2	oxygen

s the solid phase
WV water vapor

References

[1] C.K. Dyer, J. Power Sources 106 (2002) 31–34.
[2] G.J.K. Acres, J. Power Sources 100 (2001) 60–66.
[3] K. Scott, W.M. Taama, J. Cruichshank, J. Power Sources 65 (1997) 159–171.
[4] K. Scott, P. Argyropoulos, K. Sundmacher, J. Electroanal. Chem. 477 (1999) 97–110.
[5] S.F. Baxter, V.S. Battaglia, R.E. White, J. Electrochem. Soc. 146 (1999) 437–447.
[6] A.A. Kulikovsky, J. Appl. Electrochem. 30 (2000) 1005–1014.
[7] A.A. Kulikovsky, Electrochem. Commun. 5 (2003) 530–538.
[8] H. Guo, C.F. Ma, Electrochem. Commun. 6 (2004) 306–312.
[9] R. Chen, T.S. Zhao, J. Power Sources 152 (2005) 122–130.
[10] Q. Ye, T.S. Zhao, C. Xu, Electrochim. Acta 51 (2006) 5420–5429.
[11] J.B. Ge, H.T. Liu, J. Power Sources 160 (2006) 413–421.
[12] Z.H. Wang, C.Y. Wang, J. Electrochem. Soc. 150 (2003) A508–A519.
[13] J.B. Ge, H.T. Liu, J. Power Sources 163 (2007) 907–915.
[14] J. Divisek, J. Fuhrmann, K. Gartner, R. Jung, J. Electrochem. Soc. 150 (2003) A811–A825.
[15] W.W. Yang, T.S. Zhao, Electrochim. Acta 52 (2007) 6125–6140.
[16] W.W. Yang, T.S. Zhao, C. Xu, Electrochim. Acta 53 (2007) 853–862.
[17] W.W. Yang, T.S. Zhao, J. Power Sources 174 (2007) 136–147.
[18] R. Chen, T.S. Zhao, W.W. Yang, C. Xu, J. Power Sources 175 (2008) 276–287.
[19] C. Xu, T.S. Zhao, W.W. Yang, J. Power Sources 178 (2008) 291–308.
[20] X.G. Yang, F.Y. Zhang, A.L. Lubawy, C.Y. Wang, Electrochem. Solid-State Lett. 7 (2004) A408–A411.
[21] H. Yang, T.S. Zhao, Q. Ye, J. Power Sources 139 (2005) 79–90.
[22] C.W. Wong, T.S. Zhao, Q. Ye, J.G. Liu, J. Electrochem. Soc. 152 (2005) A1600–A1605.
[23] D. Spernjak, A.K. Prasad, S.G. Advani, J. Power Sources 170 (2007) 334–344.
[24] E. Middelman, Fuel Cell Bull. 2002 (2002) 9–12.
[25] J. Giner, C. Hunter, J. Electrochem. Soc. 116 (8) (1969) 1124–1130.
[26] N.P. Siegel, M.W. Ellis, D.J. Nelson, M.R. von Spakovsky, J. Power Sources 115 (2003) 81–89.
[27] Q. Wang, M. Eikerling, D. Song, Z. Liu, J. Electroanal. Chem. 573 (2004) 61–69.
[28] Q. Wang, D. Song, T. Navessin, S. Holdcroft, Z. Liu, Electrochim. Acta 50 (2004) 725–730.
[29] W. Sun, B.A. Peppley, K. Karan, Electrochim. Acta 50 (2005) 3359–3374.
[30] C.Y. Du, T. Yang, P.F. Shi, G.P. Yin, X.Q. Cheng, Electrochim. Acta 51 (2006) 4934–4941.
[31] J. Nordlund, G. Lindbergh, J. Electrochem. Soc. 149 (2002) A1107–A1113.
[32] M.C. Leverette, Trans. AIME 142 (1941) 152–169.
[33] U. Pasaogullari, C.Y. Wang, J. Electrochem. Soc. 151 (2004) A399–A406.
[34] W.Q. Tao, Numerical Heat Transfer, second ed., Xi'an Jiaotong University Press, Xi'an, 2001, 5–6.
[35] T. Wilmarth, M. Ishii, Int. J. Heat Mass Transfer 37 (1994) 1749–1758.
[36] G. Work, M. Dreyer, H.J. Rath, Int. J. Multiphas. Flow 26 (2000) 1037–1061.
[37] C. Xu, Y.L. He, T.S. Zhao, R. Chen, Q. Ye, J. Electrochem. Soc. 153 (2006) A1358–A1364.
[38] S. Um, C.Y. Wang, K.S. Chen, J. Electrochem. Soc. 147 (2000) 4485–4493.
[39] D. Song, Q. Wang, Z. Liu, T. Navessin, M. Eikerling, S. Holdcroft, J. Power Sources 126 (2004) 104–111.
[40] G. Murgia, L. Pisani, A.K. Shula, K. Scott, J. Electrochem. Soc. 150 (2003) A1231–A1245.